



Stable p-block metals electronic perturbation in PtM@CNT (M=Ga, In, Pb and Bi) for acidic seawater hydrogen production at commercial current densities

Nanzhu Nie ^{a,b}, Dan Zhang ^{a,b}, Zuochao Wang ^a, Shijie Ge ^b, Yanli Gu ^a, Bo Yang ^b, Jianping Lai ^{a,*}, Lei Wang ^{a,b, **}

^a Key Laboratory of Eco-chemical Engineering, Ministry of Education, International Science and Technology Cooperation Base of Eco-chemical Engineering and Green Manufacturing, College of Chemistry and Molecular Engineering, Qingdao University of Science and Technology, Qingdao 266042, PR China

^b Shandong Engineering Research Center for Marine Environment Corrosion and Safety Protection, College of Environment and Safety Engineering, Qingdao University of Science and Technology, Qingdao 266042, PR China



ARTICLE INFO

Keywords:

Alloy
Electronic regulation
Seawater
HER
Electrocatalyst

ABSTRACT

Achieving acidic seawater hydrogen production under commercial current densities remains a challenge. We present here a novel strategy through strong metal-support interaction (SMSI) and Pt-p-block alloys (PtM@CNT, M = Ga, In, Pb, and Bi) to construct a stable electronic perturbation and achieve acidic seawater hydrogen evolution performance at commercial current densities for the first time. SMSI stabilizes electronic perturbation and promotes durability up to 360 h. The optimized Pt₆₁Ga₃₉@CNT exhibits an overpotential of 18 mV at 10 mA cm⁻² in 0.5 M H₂SO₄ and maintains 360 h stability at 500 mA cm⁻² in acidic seawater. Density functional theory (DFT) calculation reveals that the optimized σ -band center of Pt and ΔG_{H^+} increase the catalytic activity, and the higher vacancy formation energy enhances the durability. Overall, this discovery not only first achieves stable acidic seawater hydrogen production under commercial current densities, but also opens a new opportunity to explore catalytic applications of p-block alloys and SMSI stabilized electronic perturbation.

1. Introduction

In response to global climate change and the rapid consumption of fossil fuels, the concept of hydrogen economy was proposed as a vision of the future economic structure [1,2]. As the popularity of renewable electricity, combining renewable electricity with electrochemical processes to produce hydrogen has attracted a lot of interest from academia and industry [3–7]. The arid coastal area is the preferred place to produce electrolytic hydrogen using renewable power, possesses sufficient photovoltaic and wind power potentials [8–11]. However, a large supply of freshwater will limit the electrolytic water technology for wider applications. Acidic electrolytes exhibit higher hydrogen evolution reaction (HER) kinetics due to the high concentrations of protons/hydronium ions [12,13]. Developing hydrogen production technology with acidic seawater as the electrolyte may solve the

problem of fresh water shortage and increase production capacity. Because of corrosive ions and acidic media, long-term stability under commercial current densities acidic seawater HER has not been realized [14,15]. Therefore, it is necessary to develop stable catalysts for acidic seawater hydrogen evolution at commercial current densities.

So far, platinum (Pt) plays an irreplaceable role in acidic HER [16, 17]. However, its high price, scarcity and poor stability severely restrict the practical application. Pt has a strong H adsorption activity, so its electronic structure should be adjusted to reduce the binding energy [18–20]. Many feasible strategies have been used to modulate the electronic structure of Pt including alloying [21], coordination regulation [22], crystal adjustment [23], strain engineering [24], etc. Among them, alloying strategy can not only adjust the electronic structure of Pt but also reduce the loading. Alloying Pt with 3d transition metals (such as Fe, Co, Ni) has been widely explored at present [25–27].

* Corresponding author.

** Corresponding author at: Key Laboratory of Eco-chemical Engineering, Ministry of Education, International Science and Technology Cooperation Base of Eco-chemical Engineering and Green Manufacturing, College of Chemistry and Molecular Engineering, Qingdao University of Science and Technology, Qingdao 266042, PR China.

E-mail addresses: jplai@qust.edu.cn (J. Lai), inorchemwl@126.com (L. Wang).

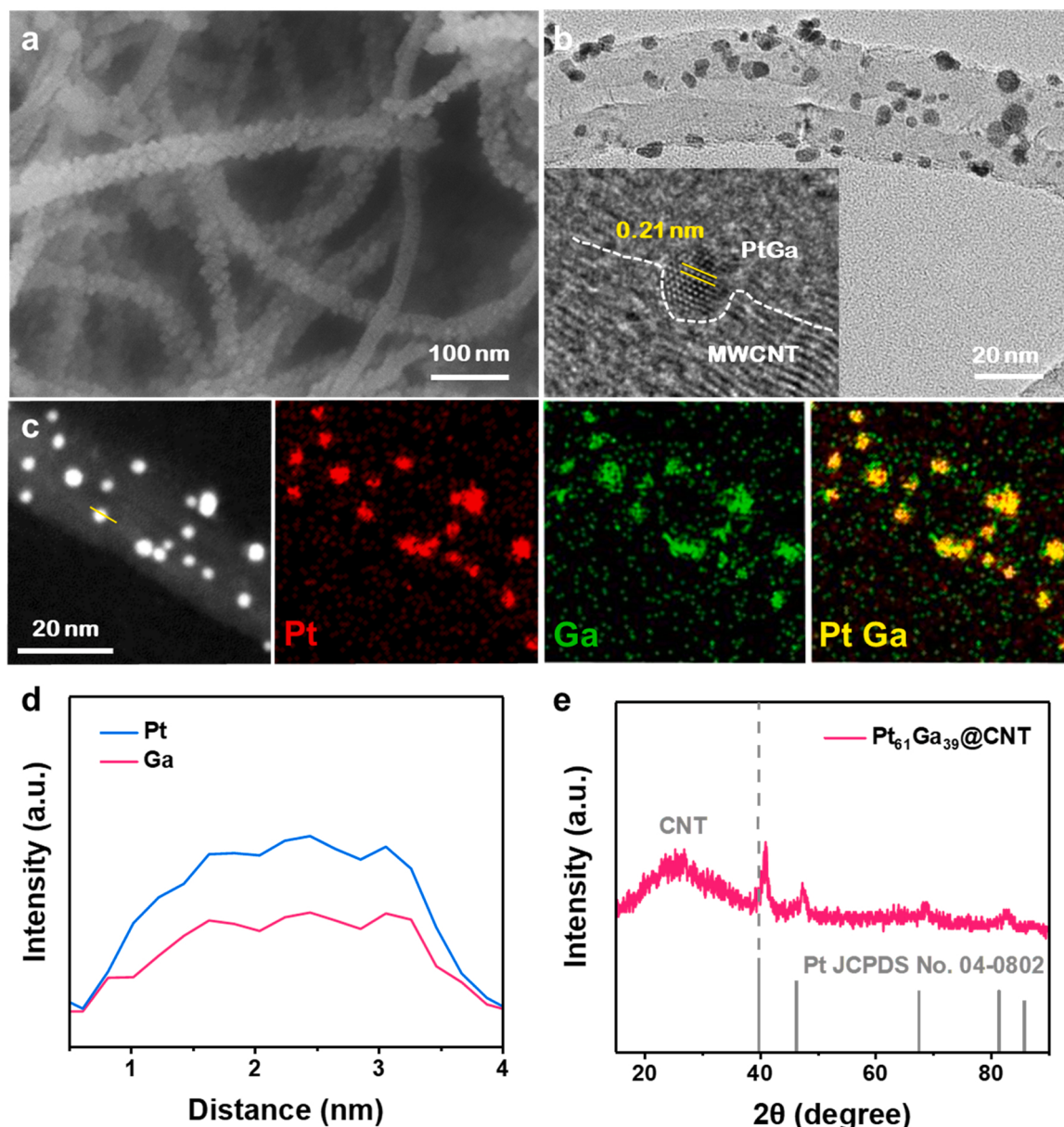


Fig. 1. Characterization of $\text{Pt}_{61}\text{Ga}_{39}@\text{CNT}$. (a) SEM image. (b) TEM image (HR-TEM insert). (c) Corresponding TEM mapping. (d) Corresponding TEM line-scanning. (e) XRD pattern.

Nevertheless, these catalysts cannot be stable under harsh conditions (commercial current densities and acidic seawater environment) due to the rapid leaching of reactive transition metals [28]. P-block metals with closed d^{10} electronic configurations are more stable than 3d transition metals and can regulate the electronic structure of Pt [29–32]. In addition, SMSI can not only stabilize the electron transfer but also prevent agglomeration and etching of nanomaterials [33,34]. This inspired us that SMSI combined with Pt-p-block alloys can solve the above problems.

Here, we present a novel strategy through SMSI and Pt-p-block alloys ($\text{PtM}@\text{CNT}$, M = Ga, In, Pb and Bi) to construct a stable electronic perturbation and achieve acidic seawater hydrogen production performance at commercial current densities for the first time. SMSI stabilizes electron transport and promotes durability. The optimized $\text{PtGa}@\text{CNT}$ also exhibits superior hydrogen evolution reaction (HER) properties in acidic, alkalic and acidic brine electrolytes. DFT calculation deeply reveals that the electronic perturbation of Ga on Pt increases the hydrogen adsorption capacity, thereby reducing the reaction activation energy.

And the higher vacancy formation energy in $\text{PtGa}@\text{CNT}$ leads to a better stability.

2. Methods and experimental section

2.1. Chemicals

Platinum (II) 2,4-pentanedionate ($\text{Pt}(\text{acac})_2$, 97%) was obtained from Sigma-Aldrich (Shanghai) Trading Co., Ltd. China. Gallium nitrate hydrate ($\text{Ga}(\text{NO}_3)_3 \cdot x\text{H}_2\text{O}$), Indium nitrate hydrate ($\text{In}(\text{NO}_3)_3 \cdot x\text{H}_2\text{O}$), lead nitrate hydrate ($\text{Pb}(\text{NO}_3)_3 \cdot x\text{H}_2\text{O}$), Bismuth nitrate hydrate ($\text{Bi}(\text{NO}_3)_3 \cdot x\text{H}_2\text{O}$), and multi-walled carbon nanotube were purchased from Shanghai Aladdin Biochemical Technology Co., Ltd. Potassium hydroxide (KOH, 90%) from Aladdin. Commercial carbon supported Pt catalyst (Pt/C , 20 wt% of 3 nm-Pt nanoparticles on carbon black) was obtained from Aladdin. Nafion solution (5%) was purchased from Sigma-Aldrich. Sulfuric acid (H_2SO_4 , 95–98%), nitric acid (HNO_3 , 95–98%) and ethanol ($\text{C}_2\text{H}_6\text{O}$) were provided by Sinopharm Chemical

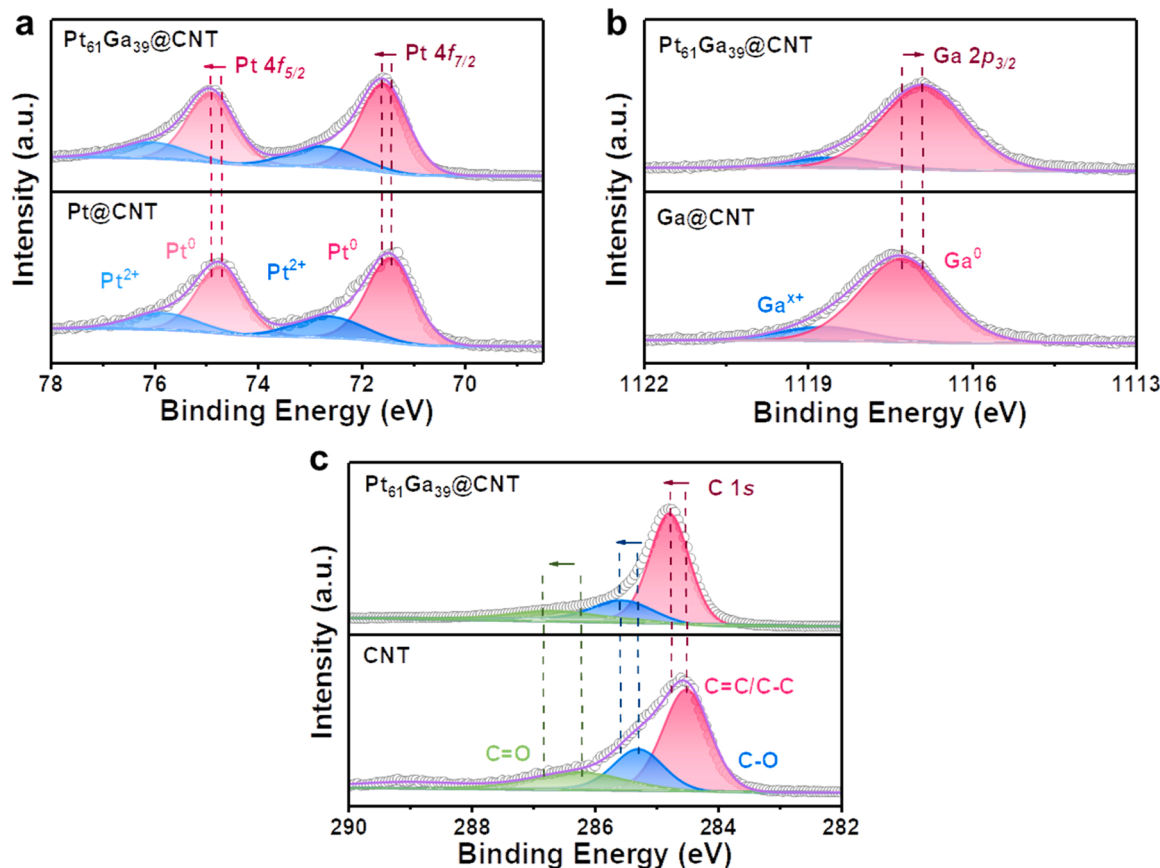


Fig. 2. XPS spectra. (a) Pt 4f of Pt₆₁Ga₃₉@CNT and Pt@CNT. (b) Ga 2p_{3/2} of Pt₆₁Ga₃₉@CNT and Ga@CNT. (c) C 1s of Pt₆₁Ga₃₉@CNT and CNT.

Reagent Co., Ltd. Ultrapure water (Millipore Milli-Q grade) with a resistivity of 18.2 MΩ was used in all the experiments.

2.2. Synthesis of PtM@CNT

All catalysts were synthesized using a solvent-free microwave method. Taking Pt₆₁Ga₃₉ @CNT, for example, Pt(acac)₂ (5 mg), Ga(NO₃)₃·xH₂O (3.4 mg), and CNT (5 mg) were mixed in a mortar and ground evenly. Put the mixture into a 10 mL quartz vial, pour Ar into the bottle. Then it was placed in a household microwave oven (Midea, PM2001) and reacted for 30 s with a power of 700 W. The synthesis is initiated at room temperature and normal atmospheric pressure. The reaction mixture was then washed and centrifuged with ethanol. Finally, the product was dried overnight in a 60 °C oven to obtain a black powder.

2.3. Synthesis of Pt@CNT

The Pt@CNT was synthesized with the same procedures described above for PtM@CNT, except that there is no p-block metal salt added.

3. Results and discussions

3.1. Catalysts synthesis and physical characterizations

PtGa@CNT catalysts were synthesized by a simple solvent-free microwave reaction in a domestic microwave oven for 30 s (Fig. S1). Three samples of PtGa@CNT with different proportions (atomic ratios of Pt/Ga: 0.5, 1.5, and 2.0) were determined by inductively coupled plasma atomic emission spectroscopy (ICP-AES) (Table S1). Among them, the PtGa@CNT catalyst with an atomic ratio of 1.5 gave the best HER

activity in 0.5 M H₂SO₄ solution (Fig. S2). We employed a scanning electron microscope (SEM) and transmission electron microscope (TEM) to study the morphology and structure of the Pt₆₁Ga₃₉ @CNT. PtGa nanoparticles with very high density are grown on CNT, and feature an average size of about 3.0 nm (Fig. 1a, S3 and S4). The Pt₆₁Ga₃₉ @CNT was further confirmed by the high-resolution transmission electron microscopy (HR-TEM) image (Fig. 1b). The lattice spacing for PtGa (0.21 nm) is smaller than that of Pt (111) plane (0.22 nm). This confirms that Pt and Ga are alloyed inducing a compressive strain, which might influence the electrochemical activity. Due to the instantaneous high temperature of microwave reaction, PtGa alloy is anchored on CNT with coating layer which preliminarily believed that SMSI is produced. Moreover, the elemental mapping and line-scanning acquired by energy-dispersive X-ray spectroscopy (EDS) analysis show that Pt and Ga are uniformly dispersed with an atomic ratio of 1.5, which was consistent with the ICP result (Fig. 1c-d and S5). And the weight percent of PtGa in the catalyst Pt₆₁Ga₃₉ @CNT is about 18 wt%. Additionally, the X-ray diffraction (XRD) pattern (Fig. 1e) of Pt₆₁Ga₃₉ @CNT shows that the characteristic diffraction peaks index well with face-centered cubic (fcc) Pt. It is worth noting that the diffraction peak of Pt₆₁Ga₃₉ @CNT is slightly shifted to a higher angle region compared to the standard card of Pt, which is generated due to the lattice contraction initiated by the incorporation of Ga (122 pm) with smaller atomic radius into Pt (139 pm) [35]. The change can be attributed to the formation of a Pt-Ga alloy with a characteristic peak at 41.1°. And the wider diffraction peaks indicate a smaller dimension, further demonstrating the ultrafine properties of these catalysts [36]. The broad peak from 20° to 40° is assigned to CNT (Fig. S6). The composition and unique electronic structure were further investigated by X-ray photoelectron spectroscopy (XPS). It confirms the presence of Pt and Ga elements in Pt₆₁Ga₃₉ @CNT catalyst with an atomic ratio of 1.5 (Fig. S7). As shown in Fig. 2a, Pt 4f

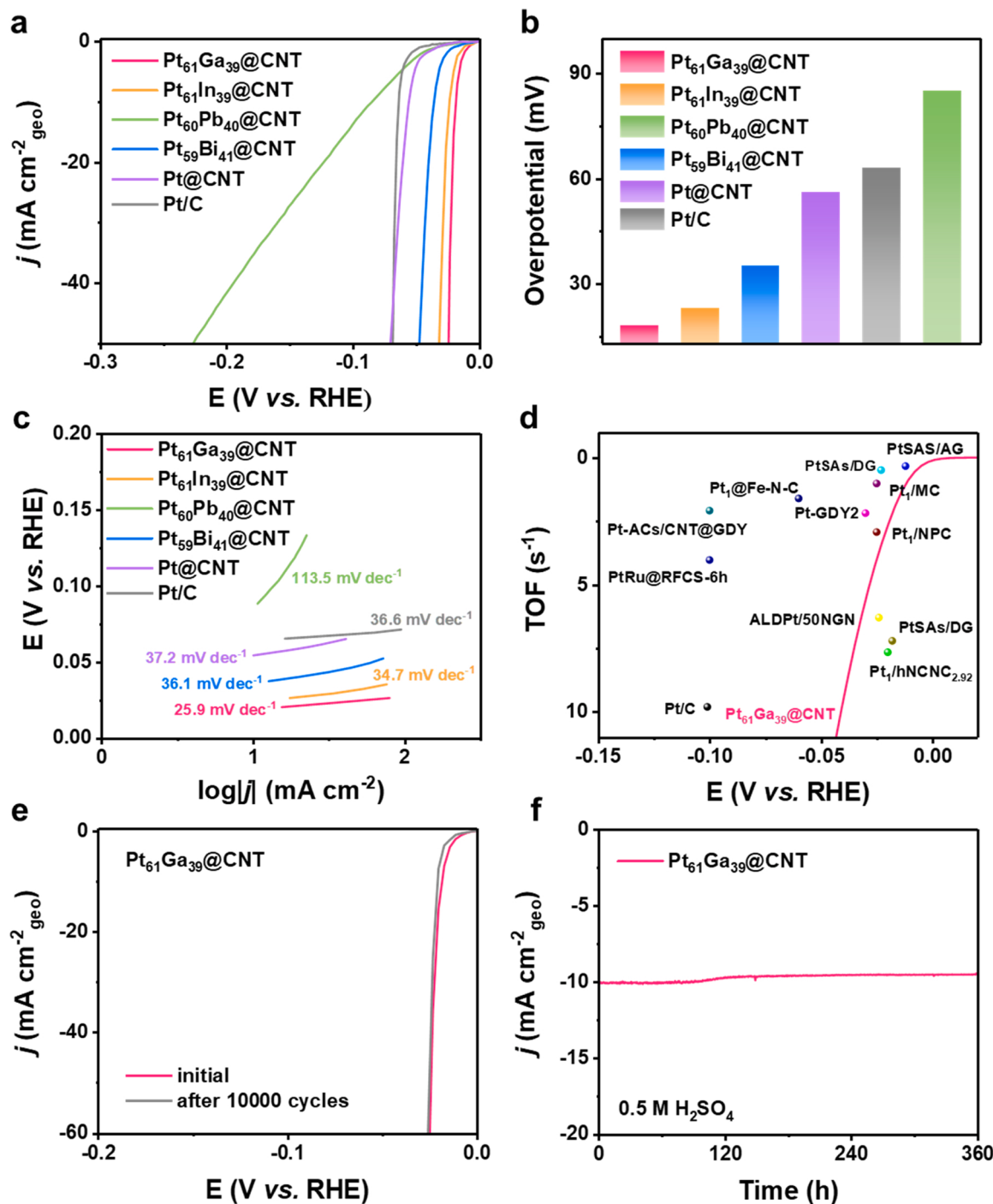


Fig. 3. Electrochemical HER performance for PtM@CNT, Pt@CNT and commercial Pt/C in 0.5 M H₂SO₄ electrolyte. (a) Polarization curves. (b) Overpotentials at 10 mA cm⁻². (c) Tafel plots. (d) TOF of Pt₆₁Ga₃₉@CNT and the comparison with the literatures. Pt/C, Pt₁/OLC [45], Pt₁/hNCNC_{2.92} [46], PtSAs/AG [47], PtSAs/DG [48], Pt-GDY₂ [49], ALDpt/50NGN [50], Pt-GT-1 [51], Pt₁@Fe-N-C [52], Pt₁/MC [53], Pt₁/NPC [54], PtSA/C-Air [19], Pt-ACs/CNT@GDY [55], PtRu@RFCS-6 h [56]. (e) Polarization curves before and after 10,000 CV cycles from 0.01 to -0.02 V vs. RHE. (f) Chronoamperometry curve at -0.018 V vs. RHE.

signal is deconvolved into two species (Pt⁰ and Pt²⁺). The dominant metallic Pt signals for Pt₆₁Ga₃₉@CNT at 71.57 eV and 74.91 eV are obtained. Meanwhile, the two peaks at 72.73 eV and 76.05 eV correspond to Pt²⁺. Interestingly, the characteristic peaks for the Pt₆₁Ga₃₉@CNT are significantly shifted to higher binding energies than Pt. This positive shift is likely due to the introduction of Ga atoms in Pt lattice, causing the electron transformation from Pt to Ga and the valence d-band center shift [37]. Besides, the Ga 2p_{3/2} binding energies are 1116.88 eV for the zerovalent state and 1118.53 eV for the oxidized ones (Fig. 2b). The C 1 s peak of Pt₆₁Ga₃₉@CNT shifts to higher binding

energy compared to CNT, which further verified SMSI phenomenon (Fig. 2c). Solvent free microwave method can also be extended to synthesize different components of PtM@CNT (M= Ga, In, Pb and Bi) alloy catalysts. The other PtM@CNT catalysts possess similar morphology and structure by SEM, TEM, XRD, and XPS characterizations. And the surface elements ratios of Pt/M are all about 1.5 (measured by XPS). These results prove the successful formation of PtM@CNT (Fig. S8-S13). Pt@CNT is synthesized as a contrast material (Fig. S14).

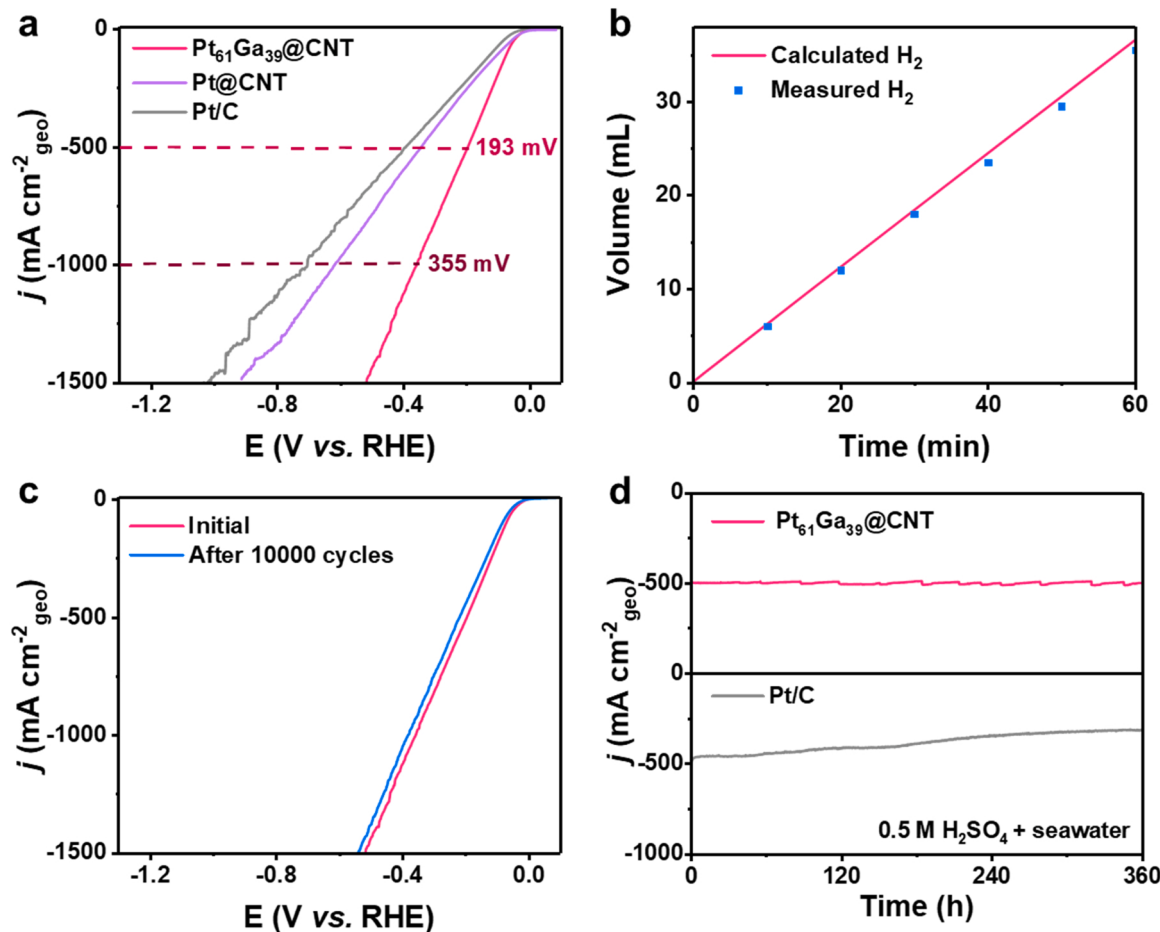


Fig. 4. Electrochemical HER performance for $\text{Pt}_{61}\text{Ga}_{39}@\text{CNT}$, $\text{Pt}@\text{CNT}$ and commercial Pt/C in $0.5 \text{ M H}_2\text{SO}_4 + \text{real seawater}$ electrolyte at high current densities. (a) Polarization curves. (b) Theoretical and experimental results of H_2 production for $\text{Pt}_{61}\text{Ga}_{39}@\text{CNT}$. (c) Polarization curves before and after 10,000 CV cycles from 0 to -0.15 V vs. RHE for $\text{Pt}_{61}\text{Ga}_{39}@\text{CNT}$. (d) Chronoamperometry curves (-0.193 V vs. RHE for $\text{Pt}_{61}\text{Ga}_{39}@\text{CNT}$, -0.389 V vs. RHE for Pt/C).

3.2. Electrocatalytic properties measurement

Fig. 3a shows linear scanning voltammograms (LSVs) with 95% iR in $0.5 \text{ M H}_2\text{SO}_4$ electrolyte, which increases in the following order: $\text{Pt}_{61}\text{Ga}_{39} @\text{CNT} > \text{Pt}_{61}\text{In}_{39} @\text{CNT} > \text{Pt}_{59}\text{Bi}_{41} @\text{CNT} > \text{Pt}@\text{CNT} > \text{commercial Pt/C (20 wt\%)} > \text{Pt}_{60}\text{Pb}_{40} @\text{CNT}$ (Fig. S15). The overpotential of $\text{Pt}_{61}\text{Ga}_{39} @\text{CNT}$ is 18 mV at a current density of 10 mA cm^{-2} , which is 46 mV lower than commercial Pt/C (30 mV) (Fig. 3b). $\text{Pt}_{61}\text{Ga}_{39} @\text{CNT}$ exhibits a comparable onset potential (9 mV) to commercial Pt/C (16 mV). The Tafel slope of $\text{Pt}_{61}\text{Ga}_{39} @\text{CNT}$ (25.9 mV dec^{-1}) is minimal (Fig. 3c). And the slope derived from the steady-state polarization curve is shown in Fig. S16. This identifies a Volmer-Tafel mechanism, while the rate-determining step is the recombination of surface adsorbed hydrogen atoms. In this case, the HER proceeds through the combination of two adsorbed hydrogen atoms on $\text{Pt}_{61}\text{Ga}_{39} @\text{CNT}$ to form molecular hydrogen. And the exchange current density (j_0) of $\text{Pt}_{61}\text{Ga}_{39} @\text{CNT}$ is the highest (1.05 mA cm^{-2}). In addition, the mass activity of $\text{Pt}_{61}\text{Ga}_{39} @\text{CNT}$ is $14.2 \text{ A mg}_{\text{Pt}}^{-1}$ at 70 mV, which performs best compared with the other catalysts (Fig. S17). To understand the specific activities of the catalysts, the electrochemical active surface areas (ECSAs) were calculated according to the underpotential desorption of hydrogen (H-UPD) (Fig. S18). $\text{Pt}_{61}\text{Ga}_{39} @\text{CNT}$ reaches $78.5 \text{ m}^2/\text{g}_{\text{Pt}}$ of ECSA, which is larger than commercial Pt/C ($71.4 \text{ m}^2/\text{g}_{\text{Pt}}$) (Fig. S19). Also, the ECSAs of $\text{Pt}_{61}\text{Ga}_{39} @\text{CNT}$ measured by CO stripping (Fig. S20) and underpotentially deposited of Cu (Cu-UPD) (Fig. S21) experiments are $86.4 \text{ m}^2/\text{g}_{\text{Pt}}$ and $98.3 \text{ m}^2/\text{g}_{\text{Pt}}$ respectively. The number of active sites (n)

calculated by Cu-UPD of $\text{Pt}_{61}\text{Ga}_{39} @\text{CNT}$ is $2.1 * 10^{-3} \text{ mol/g}_{\text{Pt}}$, which is higher than commercial Pt/C ($1.6 * 10^{-3} \text{ mol/g}_{\text{Pt}}$) [38]. Moreover, $\text{Pt}_{61}\text{Ga}_{39} @\text{CNT}$ displays an advantageous specific activity of 81.6 mA cm^{-2} at 70 mV (normalized by H-UPD) (Fig. S22). The TOF value of $\text{Pt}_{61}\text{Ga}_{39} @\text{CNT}$ reaches 37.34 s^{-1} at 100 mV, which can outperform the most reported catalysts (Fig. 3d and S23). Electrochemical double-layer capacitance (C_{dl}) calculated by CV tests at different scan rates are shown in Fig. S24. Next, the H_2 produced during the reaction was collected and tested by gas chromatography, and the Faraday efficiency is close to 100% (Fig. S25). A detailed comparison of Pt-based HER catalysts in $0.5 \text{ M H}_2\text{SO}_4$ electrolyte is listed in Table S2. The 10,000 cyclic voltammetry (CV) cycles (Fig. 3e) and chronoamperometry (Fig. 3f) measurements observe that $\text{Pt}_{61}\text{Ga}_{39} @\text{CNT}$ demonstrates a high degree of durability in an acidic medium. After the stability test, we conducted SEM, TEM, XRD, and XPS characterizations of the electrocatalyst (Figs. S26 and S27), and found that the morphological feature and structure are basically maintained. Additionally, there is a minor leaching of Ga from the surface of the catalyst after long-term HER stability test (Table S3).

Further, we test the HER performance of $\text{PtM}@\text{CNT}$ ($\text{M} = \text{Ga, In, Pb and Bi}$) in 1.0 M KOH electrolyte. $\text{Pt}_{61}\text{Ga}_{39} @\text{CNT}$ reaches the smallest overpotential (20 mV at 10 mA cm^{-2}), Tafel slope (31.7 mV dec^{-1}) and the TOF of 21.33 s^{-1} at 100 mV (Figs. S28 and S29). At the same time, $\text{Pt}_{61}\text{Ga}_{39} @\text{CNT}$ shows satisfactory mass activity (Fig. S30) and specific activity (Fig. S31). C_{dl} value is the highest (Fig. S32). And the Faraday efficiency is close to 100% (Fig. S33). Excellent stability is also found in 1.0 M KOH (Fig. S34).

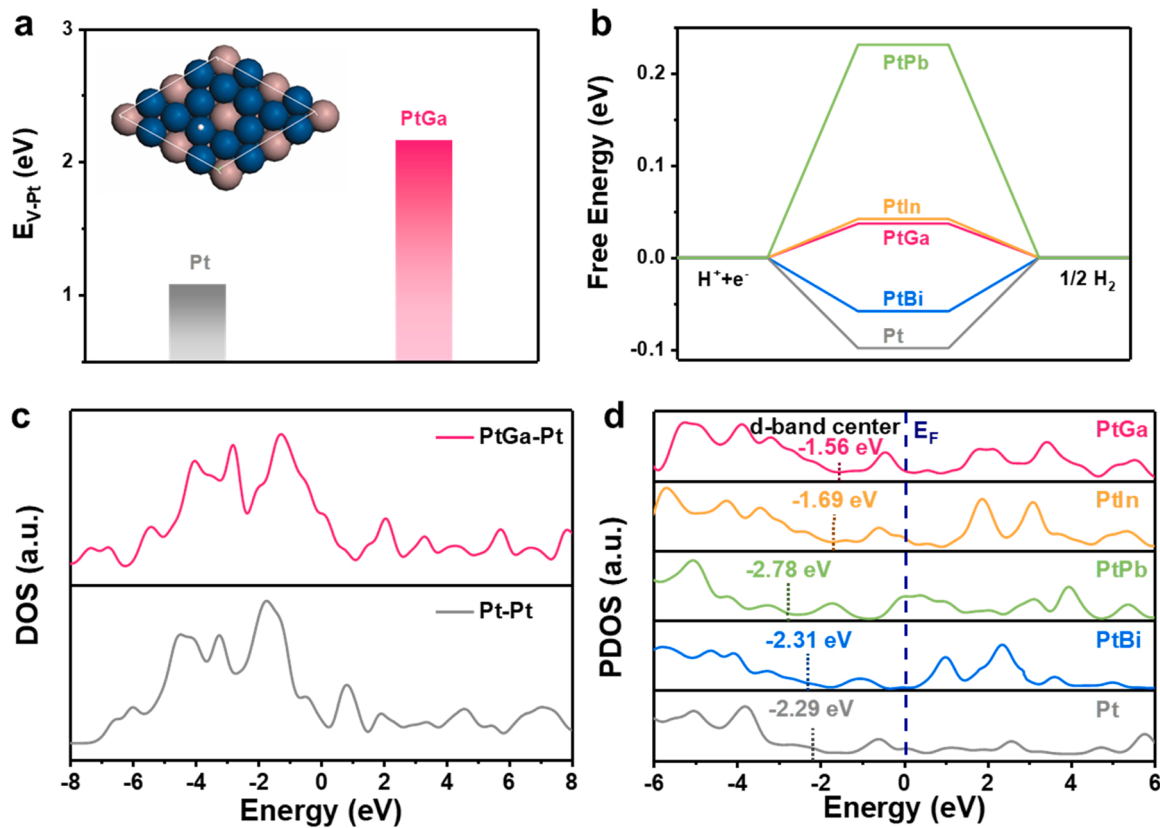


Fig. 5. DFT calculation. (a) E_{V-Pt} for Pt and PtGa, and the inset shows the crystal structure. The blue, pink and white spheres represent Pt, Ga and H atoms respectively. (b) Free-energy barriers of different catalysts. (c) DOS of Pt atoms for PtGa and Pt. (d) Calculated PDOS of different catalysts with d-band center positions.

The average salinity of seawater is about 0.599 M, mainly NaCl. Continuous electrolysis process will accumulate chloride and accelerate electrode corrosion. As shown in Fig. S35a, Pt₆₁Ga₃₉ @CNT exhibits the best HER activity in 0.5 M H₂SO₄ + 0.6 M NaCl. The overpotential of 25 mV is needed to drive a current density of 10 mA cm⁻² (Fig. S35b). The Tafel slope of Pt₆₁Ga₃₉ @CNT is 25.6 mV dec⁻¹ (Fig. S35c). Besides, Pt₆₁Ga₃₉ @CNT performs a decent mass activity (Figs. S36). To explore the catalytic performance in large-scale industrial production, Pt₆₁Ga₃₉ @CNT was dripped on a carbon cloth to obtain accurate high current density. It exhibits well in whether the acidic simulated seawater (Fig. S37) or the acidic natural seawater (Fig. 4). Pt₆₁Ga₃₉ @CNT only needs 193 mV and 355 mV to reach the current density of 500 and 1000 mA cm⁻² in 0.5 M H₂SO₄ + real seawater electrolyte (Fig. 4a). The gas amounts match well with the calculated results, indicating a nearly 100% Faradaic efficiency (Fig. 4b). Polarization curves of Pt₆₁Ga₃₉ @CNT show negligible shift relative to the initial state after 10,000 cycles (Fig. 4c). It can function for more than 360 h to maintain a current density of 500 mA cm⁻² which is more stable than commercial Pt/C (Fig. 4d). The surface morphology and crystal structure of the electrode are well maintained after the stability test (Figs. S38 and S39). In the two-electrode system, Pt₆₁Ga₃₉ @CNT||RuO₂/C was prepared by loading Pt₆₁Ga₃₉ @CNT and commercial RuO₂/C on carbon cloth as the cathode and anode. It can be seen in Fig. S40 that the Pt₆₁Ga₃₉ @CNT has a better overall seawater splitting performance than commercial Pt/C, which can reach 500 mA cm⁻² at 2.72 V.

3.3. DFT technique

DFT calculation is carried out to understand the HER reaction mechanism in acidic simulated seawater at atomistic insight. The theoretical models are constructed for PtM (M=Ga, In, Pb and Bi) based

on the corresponding structural and compositional parameters (Fig. 5a, inset). As shown in Fig. 5a, PtGa has a higher vacancy formation energy for a Pt atom (E_{V-Pt}). It suggests that the incorporation of Ga atoms increased the E_{V-Pt} , confirming the improved structural stability of PtGa@CNT. Fig. 5b shows the ΔG_{H^*} of different alloy materials, and PtGa has the Gibbs free energy closest to zero (0.037 eV). It shows that PtGa alloy is conducive to the adsorption and desorption of H, consistent with the experimental results of HER performance. As shown in Fig. 5c, the density of states (DOS) plots demonstrate that there are some new hybrid electronic states in PtGa alloy compared to pure Pt. It may be caused by the atomic hybridization between Pt and Ga [39]. And the electron-occupied state near Fermi level on PtGa is much higher than Pt, giving evidence of a stronger carrier density which is conducive to improving the hydrogen adsorption capacity [40]. This is reasonable to the obvious electron transfer in the XPS analysis results [41]. The partial densities of states (PDOS) results are shown in Fig. 5d. Compared with PtGa (-1.56 eV), d-band centers of PtIn (-1.69 eV), Pt (-2.29 eV), PtBi (-2.31 eV) and PtPb (-2.78 eV) shift farther to the Fermi level. The d-band center of the electrocatalyst has a linear relationship with the hydrogen binding energy. The higher d-band center, the stronger hydrogen binding energy of reaction intermediate on the catalyst surface (H* adsorption) [42,43]. Due to the electrons transfer from Pt to Ga and In elements, the d-band centers of PtGa and PtIn shifted positively compared with pure Pt. It indicates that the introduction of Ga or In enhances H* adsorption and promotes the Volmer step. On the contrary, the d-band center shift of PtPb is significantly negative than Pt, which means a weaker H* adsorption and inhibits the catalytic activity. And the d-band center of PtBi is similar to Pt, showing that the addition of Bi has no great influence on the H* adsorption capacity of Pt. Overall, the d-band centers of PtM have different degrees of deviation than that of Pt, indicating the electronic disturbance of p-block metals to pure Pt,

resulting in the p-d hybrid orbital [44]. Therefore, the optimized electronic structure of PtGa is more conducive to high catalytic activity.

4. Conclusion

In summary, we present a novel strategy through SMSI and Pt-p-block alloys (PtM@CNT, M = Ga, In, Pb, and Bi) to construct a stable electronic perturbation and achieve acidic seawater hydrogen evolution performance at commercial current densities for the first time. SMSI stabilizes electronic perturbation and improves the catalytic durability up to 360 h. The optimized Pt₆₁Ga₃₉@CNT requires a quite small overpotential of 18 mV to deliver a current density of 10 mA cm⁻² in 0.5 M H₂SO₄ and first achieves a low overpotential of 193 mV and 360 h stability at 500 mA cm⁻² in acidic seawater. DFT calculation reveals that PtGa has excellent ΔG_{H^*} (0.037 eV) and the closest d-band center of Pt to Fermi level. The good stability of PtGa@CNT originates from the higher vacancy formation energy. Overall, this discovery not only first achieves stable acidic seawater hydrogen production under commercial current densities, but also opens a new opportunity to explore catalytic applications of p-block alloys and SMSI stabilized electronic perturbation.

CRediT authorship contribution statement

Nanzhu Nie: Investigation, Data curation, Conceptualization, Formal analysis, Validation, Writing – original draft. **Dan Zhang:** Validation. **Zuochao Wang:** Investigation. **Shijie Ge:** Formal analysis. **Yanli Gu:** Formal analysis. **Bo Yang:** Supervision. **Jianping Lai:** Conceptualization, Writing – review, Supervision, Funding acquisition. **Lei Wang:** Funding acquisition, Supervision.

Declaration of Competing Interest

The authors declare that they have no known competing financial interests or personal relationships that could have appeared to influence the work reported in this paper.

Data availability

The authors do not have permission to share data.

Acknowledgment

This work was supported by the National Natural Science Foundation of China (51772162, 22001143, and 52072197), Youth Innovation and Technology Foundation of Shandong Higher Education Institutions, China (2019KJC004), Outstanding Youth Foundation of Shandong Province, China (ZR2019JQ14), Taishan Scholar Young Talent Program (tsqn201909114, tsqn201909123), Natural Science Foundation of Shandong Province (ZR2020YQ34), Major Scientific and Technological Innovation Project (2019JZZY020405), and Major Basic Research Program of Natural Science Foundation of Shandong Province under Grant (ZR2020ZD09).

Appendix A. Supporting information

Supplementary data associated with this article can be found in the online version at [doi:10.1016/j.apcatb.2022.122100](https://doi.org/10.1016/j.apcatb.2022.122100).

References

- [1] J.A. Turner, Sustainable hydrogen production, *Science* 305 (2004) 972, <https://doi.org/10.1126/science.1103197>.
- [2] D.M. Kammen, T.E. Lipman, Assessing the future hydrogen economy, *Science* 302 (2003) 226–229, <https://doi.org/10.1126/science.302.5643.226b>.
- [3] Z.W. Seh, J. Kibsgaard, C.F. Dickens, I. Chorkendorff, J.K. Nørskov, T.F. Jaramillo, Combining theory and experiment in electrocatalysis: insights into materials design, *Science* 355 (2017) 146, <https://doi.org/10.1126/science.aad4998>.
- [4] A. Hauch, R. Kungas, P. Blennow, A.B. Hansen, J.B. Hansen, B.V. Mathiesen, M. B. Mogensen, Recent advances in solid oxide cell technology for electrolysis, [eab6118](https://doi.org/10.1126/science.aba6118), *Science* 370 (2020), <https://doi.org/10.1126/science.aba6118>.
- [5] S. Das, S. Bhattacharjee, S. Mondal, S. Dutta, N. Bothra, S.K. Pati, S. Bhattacharyya, Bimetallic zero-valent alloy with measured high-valent surface states to reinforce the bifunctional activity in rechargeable zinc-air batteries, *ACS Sustain. Chem. Eng.* 9 (2021) 14868–14880, <https://doi.org/10.1021/acsuschemeng.1c04970>.
- [6] A. Kumar, D.K. Chaudhary, S. Parvin, S. Bhattacharyya, High performance duckweed-derived carbon support to anchor NiFe electrocatalysts for efficient solar energy driven water splitting, *J. Mater. Chem. A* 6 (2018) 18948–18959, <https://doi.org/10.1039/C8TA06946H>.
- [7] A. Sahasrabudhe, H. Dixit, R. Majee, S. Bhattacharyya, Value added transformation of ubiquitous substrates into highly efficient and flexible electrodes for water splitting, *Nat. Commun.* 9 (2018) 2014, <https://doi.org/10.1038/s41467-018-04358-7>.
- [8] S. Dresp, F. Dionigi, M. Klingenhofer, P. Strasser, Direct electrolytic splitting of seawater: opportunities and challenges, *ACS Energy Lett.* 4 (2019) 933, <https://doi.org/10.1021/acsenergylett.9b00220>.
- [9] S. Feng, Q. Fu, Expansion of global drylands under a warming climate, *Atmos. Chem. Phys.* 13 (2013) 10081, <https://doi.org/10.5194/acp-13-10081-2013>.
- [10] M. Sarno, E. Ponticorvo, D. Scarpa, Active and stable graphene supporting trimetallic alloy-based electrocatalyst for hydrogen evolution by seawater splitting, *Electrochem. Commun.* 111 (2020), 106647, <https://doi.org/10.1016/j.elecom.2019.106647>.
- [11] X. Niu, Q. Tang, B. He, P. Yang, Robust and stable ruthenium alloy electrocatalysts for hydrogen evolution by seawater splitting, *Electrochim. Acta* 208 (2016) 180–187, <https://doi.org/10.1016/j.electacta.2016.04.184>.
- [12] J. Wang, Y. Gao, H. Kong, J. Kim, S. Choi, F. Ciucci, Y. Hao, S. Yang, Z. Shao, J. Lim, Non-precious-metal catalysts for alkaline water electrolysis: operando characterizations, theoretical calculations, and recent advances, *Chem. Soc. Rev.* 49 (2020) 9154, <https://doi.org/10.1039/D0CS00575D>.
- [13] W. Zhang, B. Huang, K. Wang, W. Yang, F. Lv, N. Li, Y. Chao, P. Zhou, Y. Yang, Y. Li, J. Zhou, W. Zhang, Y. Du, D. Su, S. Guo, WO_x-surface decorated PtNi@Pt dendritic nanowires as efficient pH-universal hydrogen evolution electrocatalysts, *Adv. Energy Mater.* 11 (2021), 2003192, <https://doi.org/10.1002/aenm.202003192>.
- [14] Z. Pu, I.S. Amiinu, Z. Kou, W. Li, S. Mu, RuP₂-based catalysts with platinum-like activity and higher durability for hydrogen evolution reaction at all pH values, *Angew. Chem. Int. Ed.* 56 (2017) 11559, <https://doi.org/10.1002/anie.201704911>.
- [15] L. Zhao, Y. Zhang, Z. Zhao, Q. Zhang, L. Huang, L. Gu, G. Lu, J. Hu, L. Wan, Steering elementary steps towards efficient alkaline hydrogen evolution via size-dependent Ni/NiO nanoscale heterosurfaces, *Natl. Sci. Rev.* 7 (2020) 27–36, <https://doi.org/10.1093/nsr/nwz145>.
- [16] S. Park, Y.-L. Lee, Y. Yoon, S.Y. Park, S. Yim, W. Song, S. Myung, K.-S. Lee, H. Chang, S.S. Lee, K.-S. An, Reducing the high hydrogen binding strength of vanadium carbide MXene with atomic Pt confinement for high activity toward HER, *Appl. Catal. B Environ.* 304 (2022), 120989, <https://doi.org/10.1016/j.apcatb.2021.120989>.
- [17] J.N. Hansen, H. Prats, K.K. Toudahl, N. Mørch Secher, K. Chan, J. Kibsgaard, I. Chorkendorff, Is there anything better than Pt for HER, *ACS Energy Lett.* 6 (2021) 1175–1180, <https://doi.org/10.1021/acsenergylett.1c00246>.
- [18] J. Dai, Y. Zhu, Y. Chen, X. Wen, M. Long, X. Wu, Z. Hu, D. Guan, X. Wang, C. Zhou, Q. Lin, Y. Sun, S.C. Weng, H. Wang, W. Zhou, Z. Shao, Hydrogen spillover in complex oxide multifunctional sites improves acidic hydrogen evolution electrocatalysis, *Nat. Commun.* 13 (2022) 1189, <https://doi.org/10.1038/s41467-022-28843-2>.
- [19] J. Li, Y. Zhou, W. Tang, J. Zheng, X. Gao, N. Wang, X. Chen, M. Wei, X. Xiao, W. Chu, Cold-plasma technique enabled supported Pt single atoms with tunable coordination for hydrogen evolution reaction, *Appl. Catal. B Environ.* 285 (2021), 119861, <https://doi.org/10.1016/j.apcatb.2020.119861>.
- [20] R. Majee, A. Kumar, T. Das, S. Chakraborty, S. Bhattacharyya, Tweaking nickel with minimal silver in a heterogeneous alloy of decahedral geometry to deliver platinum-like hydrogen evolution activity, *Angew. Chem. Int. Ed.* 59 (2020) 2881–2889, <https://doi.org/10.1002/anie.201913704>.
- [21] H. Li, Y. Han, H. Zhao, W. Qi, D. Zhang, Y. Yu, W. Cai, S. Li, J. Lai, B. Huang, L. Wang, Fast site-to-site electron transfer of high-entropy alloy nanocatalyst driving redox electrocatalysis, *Nat. Commun.* 11 (2020) 5437, <https://doi.org/10.1038/s41467-020-19277-9>.
- [22] J. Zhong, K. Huang, W. Xu, H. Tang, M. Waqas, Y. Fan, R. Wang, W. Chen, Y. Wang, New strategy of S,N co-doping of conductive-copolymer-derived carbon nanotubes to effectively improve the dispersion of PtCu nanocrystals for boosting the electrocatalytic oxidation of methanol, *Chin. J. Catal.* 42 (2021) 1205–1215, [https://doi.org/10.1016/S1872-2067\(20\)63748-2](https://doi.org/10.1016/S1872-2067(20)63748-2).
- [23] L. Huang, H. Lin, C.Y. Zheng, E.J. Kluender, R. Golnabi, B. Shen, C.A. Mirkin, Multimetallic high-index faceted heterostructured nanoparticles, *J. Am. Chem. Soc.* 142 (2020) 4570–4575, <https://doi.org/10.1021/jacs.0c00045>.
- [24] L. Gao, T. Sun, X. Tan, M. Liu, F. Xue, B. Wang, J. Zhang, Y. Lu, C. Ma, H. Tian, S. Yang, S.C. Smith, H. Huang, Trace doping of early transition metal enabled efficient and durable oxygen reduction catalysis on Pt-based ultrathin nanowires, *Appl. Catal. B Environ.* 303 (2022), 120918, <https://doi.org/10.1016/j.apcatb.2021.120918>.

[25] Q. Cheng, S. Yang, C. Fu, L. Zou, Z. Zou, Z. Jiang, J. Zhang, H. Yang, High-loaded sub-6 nm Pt₁Co₁ intermetallic compounds with highly efficient performance expression in PEMFCs, *Energy Environ. Sci.* 15 (2022) 278–286, <https://doi.org/10.1039/D1EE02530A>.

[26] W. Tong, B. Huang, P. Wang, Q. Shao, X. Huang, Exposed facet-controlled N₂ electroreduction on distinct Pt₃Fe nanostructures of nanocubes, nanorods and nanowires, *nwa088*, *Natl. Sci. Rev.* 8 (2021), <https://doi.org/10.1093/nsr/nwa088>.

[27] Q. Zhang, Y. Kuang, Y. Li, M. Jiang, Z. Cai, Y. Pang, Z. Chang, X. Sun, Synthesis and performance optimization of ultrathin two-dimensional CoFePt alloy materials via in situ topotactic conversion for the hydrogen evolution reaction, *J. Mater. Chem. A* 7 (2019) 9517–9522, <https://doi.org/10.1039/C9TA02010A>.

[28] Z. Cai, Z. Wang, Y. Xia, H. Lim, W. Zhou, A. Taniguchi, M. Ohtani, K. Kobiro, T. Fujita, Y. Yamauchi, Tailored catalytic nanoframes from metal-organic frameworks by anisotropic surface modification and etching for the hydrogen evolution reaction, *Angew. Chem. Int. Ed.* 60 (2021) 4747, <https://doi.org/10.1002/anie.20201618>.

[29] T. Wang, X. Cao, H. Qin, L. Shang, S. Zheng, F. Fang, L. Jiao, P-Block atomically dispersed antimony catalyst for highly efficient oxygen reduction reaction, *Angew. Chem. Int. Ed.* 60 (2021) 21237–21241, <https://doi.org/10.1002/anie.202108599>.

[30] L. Gao, X. Li, Z. Yao, H. Bai, Y. Lu, C. Ma, S. Lu, Z. Peng, J. Yang, A. Pan, H. Huang, Unconventional p-d hybridization interaction in PtGa ultrathin nanowires boosts oxygen reduction electrocatalysis, *J. Am. Chem. Soc.* 141 (2019) 18083–18090, <https://doi.org/10.1021/jacs.9b07238>.

[31] Y. Zhu, L. Bu, Q. Shao, X. Huang, Structurally ordered Pt₃Sn nanofibers with highlighted antipoisoning property as efficient ethanol oxidation electrocatalysts, *ACS Catal.* 10 (2020) 3455–3461, <https://doi.org/10.1021/acscatal.9b04313>.

[32] J. Zhang, M. Yuan, T. Zhao, W. Wang, H. Huang, K. Cui, Z. Liu, S. Li, Z. Li, G. Zhang, Cu-incorporated PtBi intermetallic nanofiber bundles enhance alcohol oxidation electrocatalysis with high CO tolerance, *J. Mater. Chem. A* 9 (2021) 20676–20684, <https://doi.org/10.1039/D1TA06015E>.

[33] J. Zhang, D. Zhu, J. Yan, C. Wang, Strong metal-support interactions induced by an ultrafast laser, *Nat. Commun.* 12 (2021) 6665, <https://doi.org/10.1038/s41467-021-27000-5>.

[34] Q. Li, X. Wang, Z. Xie, X. Peng, L. Guo, X. Yu, X. Yang, Z. Lu, X. Zhang, L. Li, Polar bonds induced strong Pd-support electronic interaction drives remarkably enhanced oxygen reduction activity and stability, *Appl. Catal. B Environ.* 305 (2022), 121020, <https://doi.org/10.1016/j.apcatb.2021.121020>.

[35] Q. Feng, S. Zhao, D. He, S. Tian, L. Gu, X. Wen, C. Chen, Q. Peng, D. Wang, Y. Li, Strain engineering to enhance the electrooxidation performance of atomic-layer Pt on intermetallic Pt₃Ga, *J. Am. Chem. Soc.* 140 (2018) 2773, <https://doi.org/10.1021/jacs.7b13612>.

[36] J. Lai, F. Lin, Y. Tang, P. Zhou, Y. Chao, Y. Zhang, S. Guo, Efficient bifunctional polyalcohol oxidation and oxygen reduction electrocatalysts enabled by ultrathin PtPdM (M = Ni, Fe, Co) nanosheets, *Adv. Energy Mater.* 9 (2019), 1800684, <https://doi.org/10.1002/aenm.201800684>.

[37] J. Kim, M.K. Kabiraz, W.N. Lee, G.H. Hwang, S.I. Choi, Solvothermal doping of lanthanum on nanoscale platinum surfaces to improve oxygen electroreduction performance, *ChemElectroChem* 7 (2020) 2643, <https://doi.org/10.1002/celc.202000579>.

[38] N. Nie, D. Zhang, Z. Wang, Y. Qin, X. Zhai, B. Yang, J. Lai, L. Wang, Superfast synthesis of densely packed and ultrafine Pt-lanthanide@KB via solvent-free microwave as efficient hydrogen evolution electrocatalysts, *Small* 17 (2021), 2102879, <https://doi.org/10.1002/smll.202102879>.

[39] J. Bao, J. Wang, Y. Zhou, Y. Hu, Z. Zhang, T. Li, Y. Xue, C. Guo, Y. Zhang, Anchoring ultrafine PtNi nanoparticles on N-doped graphene for highly efficient hydrogen evolution reaction, *Catal. Sci. Technol.* 9 (2019) 4961, <https://doi.org/10.1039/C9CY01182J>.

[40] X. Li, Y. Fang, J. Wang, H. Fang, S. Xi, X. Zhao, D. Xu, H. Xu, W. Yu, X. Hai, C. Chen, C. Yao, H.B. Tao, A.G.R. Howe, S.J. Pennycook, B. Liu, J. Lu, C. Su, Ordered clustering of single atomic Te vacancies in atomically thin PtTe₂ promotes hydrogen evolution catalysis, *Nat. Commun.* 12 (2021) 2351, <https://doi.org/10.1038/s41467-021-22681-4>.

[41] H. Jin, X. Liu, A. Vasileff, Y. Jiao, Y. Zhao, Y. Zheng, S. Qiao, Single-crystal nitrogen-rich two-dimensional Mo₅N₆ nanosheets for efficient and stable seawater splitting, *ACS Nano* 12 (2018) 12767–12769, <https://doi.org/10.1021/acsnano.8b07841>.

[42] Z. Wei, H. Wang, C. Zhang, K. Xu, X.L. Lu, T.B. Lu, Reversed charge transfer and enhanced hydrogen spillover in Pt nanoclusters anchored on titanium oxide with rich oxygen vacancies boost hydrogen evolution reaction, *Angew. Chem. Int. Ed.* 60 (2021) 16622–16627, <https://doi.org/10.1002/anie.202104856>.

[43] Y. Pan, K. Sun, Y. Lin, X. Cao, Y. Cheng, S. Liu, L. Zeng, W. Cheong, D. Zhao, K. Wu, Z. Liu, Y. Liu, D. Wang, Q. Peng, C. Chen, Y. Li, Electronic structure and d-band center control engineering over M-doped CoP (M = Ni, Mn, Fe) hollow polyhedron frames for boosting hydrogen production, *Nano Energy* 56 (2019) 411–419, <https://doi.org/10.1016/j.nanoen.2018.11.034>.

[44] S. Zhang, Z. Zeng, Q. Li, B. Huang, X. Zhang, Y. Du, C. Yan, Lanthanide electronic perturbation in Pt-Lu (La, Ce, Pr and Nd) alloys for enhanced methanol oxidation reaction activity, *Energy Environ. Sci.* 14 (2021) 5911–5918, <https://doi.org/10.1039/DIEE02433G>.

[45] D. Liu, X. Li, S. Chen, H. Yan, C. Wang, C. Wu, Y.A. Haleem, S. Duan, J. Lu, B. Ge, P. M. Ajayan, Y. Luo, J. Jiang, L. Song, Atomically dispersed platinum supported on curved carbon supports for efficient electrocatalytic hydrogen evolution, *Nat. Energy* 4 (2019) 512–518, <https://doi.org/10.1038/s41560-019-0402-6>.

[46] Z. Zhang, Y. Chen, L. Zhou, C. Chen, Z. Han, B. Zhang, Q. Wu, L. Yang, L. Du, Y. Bu, P. Wang, X. Wang, H. Yang, Z. Hu, The simplest construction of single-site catalysts by the synergism of micropore trapping and nitrogen anchoring, *Nat. Commun.* 10 (2019) 1657, <https://doi.org/10.1038/s41467-019-09596-x>.

[47] S. Ye, F. Luo, Q. Zhang, P. Zhang, T. Xu, Q. Wang, D. He, L. Guo, Y. Zhang, C. He, X. Ouyang, M. Gu, J. Liu, X. Sun, Highly stable single Pt atomic sites anchored on aniline-stacked graphene for hydrogen evolution reaction, *Energy Environ. Sci.* 12 (2019) 1000, <https://doi.org/10.1039/C8EE02888E>.

[48] Y. Qu, B. Chen, Z. Li, X. Duan, L. Wang, Y. Lin, T. Yuan, F. Zhou, Y. Hu, Z. Yang, C. Zhao, J. Wang, C. Zhao, Y. Hu, G. Wu, Q. Zhang, Q. Xu, B. Liu, P. Gao, R. You, W. Huang, L. Zheng, L. Gu, Y. Wu, Y. Li, Thermal emitting strategy to synthesize atomically dispersed Pt metal sites from bulk Pt metal, *J. Am. Chem. Soc.* 141 (2019) 4505, <https://doi.org/10.1021/jacs.8b09834>.

[49] X. Yin, H. Wang, S. Tang, X. Lu, M. Shu, R. Si, T. Lu, Engineering the coordination environment of single-atom platinum anchored on graphdiyne for optimizing electrocatalytic hydrogen evolution, *Angew. Chem. Int. Ed.* 57 (2018) 9382, <https://doi.org/10.1002/anie.201804817>.

[50] N. Cheng, S. Stambula, D. Wang, M. Norouzi Banis, J. Liu, A. Riese, B. Xiao, R. Li, T. Sham, L. Liu, G. Botton, Xueliang, Platinum single-atom and cluster catalysis of the hydrogen evolution reaction, *Nat. Commun.* 7 (2016) 13638, <https://doi.org/10.1038/ncomms13638>.

[51] J.N. Tiwari, S. Sultan, C.W. Myung, T. Yoon, N. Li, M. Ha, A.M. Harzandi, H. J. Park, D.Y. Kim, S.S. Chandrasekaran, W.G. Lee, V. Vij, H. Kang, T.J. Shin, H. S. Shin, G. Lee, Z. Lee, K.S. Kim, Multicomponent electrocatalyst with ultralow Pt loading and high hydrogen evolution activity, *Nat. Energy* 3 (2018) 773, <https://doi.org/10.1038/s41560-018-0209-x>.

[52] X. Zeng, J. Shui, X. Liu, Q. Liu, Y. Li, J. Shang, L. Zheng, R. Yu, Single-atom to single-atom grafting of Pt₁ onto Fe-N₄ Center: Pt₁@Fe-N-C multifunctional electrocatalyst with significantly enhanced properties, *Adv. Energy Mater.* 8 (2018), 1701345, <https://doi.org/10.1002/aenm.201701345>.

[53] H. Wei, K. Huang, D. Wang, R. Zhang, B. Ge, J. Ma, B. Wen, S. Zhang, Q. Li, M. Lei, C. Zhang, J. Irawan, L. Liu, H. Wu, Iced photochemical reduction to synthesize atomically dispersed metals by suppressing nanocrystal growth, *Nat. Commun.* 8 (2017) 1490, <https://doi.org/10.1038/s41467-017-01521-4>.

[54] T. Li, J. Liu, Y. Song, F. Wang, Photochemical solid-phase synthesis of platinum single atoms on nitrogen-doped carbon with high loading as bifunctional catalysts for hydrogen evolution and oxygen reduction reactions, *ACS Catal.* 8 (2018) 8450, <https://doi.org/10.1021/acscatal.8b02288>.

[55] Y. Lv, X. Wu, H. Lin, J. Li, H. Zhang, J. Guo, D. Jia, H. Zhang, A novel carbon support: few-layered graphdiyne-decorated carbon nanotubes capture metal clusters as effective metal-supported catalysts, *Small* 17 (2021), 2006442, <https://doi.org/10.1002/smll.202006442>.

[56] K. Li, Y. Li, Y. Wang, J. Ge, C. Liu, W. Xing, Enhanced electrocatalytic performance for the hydrogen evolution reaction through surface enrichment of platinum nanoclusters alloying with ruthenium in situ embedded in carbon, *Energy Environ. Sci.* 11 (2018) 1232, <https://doi.org/10.1039/C8EE00402A>.